EES Catalysis

PAPER

View Article Online
View Journal | View Issue

Cite this: *EES Catal.*, 2025, 3, 1087

Dry reforming of methane in gliding arc plasma: bridging thermal and post-plasma catalysis†

Colin O'Modhrain, ‡*[ab] Arturo Pajares, ‡*[c] Eduardo Coutino-Gonzalez,[c] Yoran de Vos,[c] Pablo Guardia,[d] Yury Gorbanev,[ab] Bart Michielsen[c] and Annemie Bogaerts[ab]

Received 8th March 2025,
Accepted 29th May 2025

DOI: 10.1039/d5ey00067j

rsc.li/eescatalysis

This study compares thermal and post-plasma catalysis for dry reforming of methane (DRM) using nickel–alumina catalyst spheres. The optimum catalyst loading was first determined by thermo-catalytic performance testing and characterization. The selected catalyst spheres (4 wt% Ni loading) were introduced to a novel post-plasma-catalytic bed, designed to utilize the sensible heat from the plasma reactor and boost the DRM reaction without additional heating. A parametric scan of inlet CH_4 fractions (10–50 vol%) consistently shows improved CH_4 conversion in the presence of a catalyst. The CO and H_2 production rates reach peak values of *ca.* 24.4 mol mol_{Ni}^{-1} min^{-1} with 40 vol% CH_4 at the inlet, at a minimum energy cost (EC) of around 0.24 MJ per mol of reactant mixture. Interestingly, the addition of catalyst does not benefit the EC, but instead results in an improved syngas (H_2/CO) ratio for 10–30 vol% CH_4. In addition, a long-run post-plasma-catalytic test (6 h) demonstrates stable conversion and syngas ratio values. The EC obtained in this study is by far the lowest reported in post-plasma-catalytic DRM to date, and the insulated bed design reduces the heat loss from the bed and enables a more stable output. The successful coupling of a thermo-catalytic catalyst selection process with implementation in a post-plasma-catalytic bed demonstrates the coupling potential that can be realized between both research domains.

Broader context

The global shift toward carbon-neutral technologies has intensified interest in dry reforming of methane (DRM)—a process that valorises biogas, by converting methane (CH_4) and carbon dioxide (CO_2) into syngas (H_2 and CO), a crucial feedstock for fuels and chemicals. While DRM offers a sustainable alternative to fossil-based syngas production, its practical implementation is hindered by high energy requirements and catalyst deactivation from solid carbon deposition. Our research addresses this challenge with a combined experimental approach of thermal and post-plasma catalysis, where plasma activates reactant gases and generates heat. We developed an optimised Ni/Al_2O_3 catalyst, first validated under thermal conditions and then incorporated into an insulated post-plasma catalytic bed. The novel bed design ensures a more homogeneous bed temperature, which is beneficial for the endothermic DRM reaction. Our study demonstrates the lowest energy cost for post-plasma-catalytic DRM reported to date, showcasing a pathway toward more efficient DRM technology. By demonstrating the benefits of catalyst pre-screening for post-plasma applications, we highlight a viable pathway for cleaner syngas production, supporting broader efforts toward energy efficiency and carbon reduction in the chemical sector.

1. Introduction

In the context of the current global energy landscape, sustainable fuel alternatives with a zero or negative CO_2 cycle are highly desirable. Dry reforming of methane (DRM) is a process that converts methane (CH_4) and carbon dioxide (CO_2) into syngas (H_2 and CO), a valuable feedstock for fuel production and chemical synthesis (eqn (1)).[1–3] This process holds significant potential for mitigating greenhouse gas emissions by utilizing two major contributors to global warming, as well as for biogas valorisation. However, conventional thermal DRM

[a] *Research group PLASMANT, Department of Chemistry, University of Antwerp, Universiteitsplein 1, 2610 Wilrijk, Belgium. E-mail: colin.omodhrain@uantwerpen.be*
[b] *Electrification Institute, University of Antwerp, Olieweg 97, 2020 Antwerp, Belgium*
[c] *Materials & Chemistry, Flemish Institute for Technological Research (VITO NV), Boeretang 200, 2400 Mol, Belgium. E-mail: arturo.pajares@vito.be*
[d] *Institut de Ciència de Materials de Barcelona (ICMAB-CSIC), Bellaterra, 08193 Barcelona, Spain*

† Electronic supplementary information (ESI) available. See DOI: https://doi.org/10.1039/d5ey00067j

‡ These authors contributed equally.

operates at high temperatures (typically above 750 °C) and is prone to catalyst deactivation due to carbon deposition.[4–6]

$$CO_2 + CH_4 \rightleftharpoons 2CO + 2H_2 \quad \Delta_r H^\circ = 247.3 \text{ kJ mol}^{-1} \qquad (1)$$

Nickel-based catalysts are widely used in DRM due to their high catalytic activity and low industrial cost. However, carbon deposition hinders large-scale applications.[7] The size and dispersion of active metal particles significantly influence catalytic performance, with smaller Ni particle sizes effectively preventing carbon formation.[8] Al_2O_3 is a commonly used support in industrial catalysts, offering a large specific surface area and excellent thermal stability.[9] Ni serves as the active metal, facilitating the dissociation of CH_4 and CO_2, while the structured Al_2O_3 support enhances dispersion and mitigates sintering at high temperatures. However, in conventional thermal DRM, reaction temperatures above 750 °C are required to achieve high conversion rates. This leads to high energy consumption and potential catalyst deactivation over time, despite the generally reduced sintering mentioned earlier. The integration of plasma with thermal catalysis may enhance performance by utilizing plasma-generated heat and reactive species in a post-plasma-catalytic system.

As electrified processes gain traction as alternatives to conventional thermal catalysis, plasma (a partially or fully ionised gas with collective properties) emerges as a low-inertia technology, fully compatible with intermittent renewable energy sources.[10,11] Plasma catalysis can enhance conversion and selectivity in plasma-based processes by either incorporating a catalyst within the discharge zone (in-plasma catalysis, IPC) or placing it downstream from the plasma (post-plasma catalysis, PPC).

IPC benefits from short-lived reactive species in the catalyst region,[12] but requires low gas temperatures, such as those in dielectric barrier discharge (DBD) reactors, to prevent catalyst degradation.[13,14] Moreover, introducing materials into the discharge zone can alter plasma characteristics,[15,16] necessitating further study to optimize the coupled performance and achieve the potential synergy. In PPC, the catalyst is positioned downstream, allowing for higher temperatures of the plasma itself, because the catalyst is spatially separated from it, thus avoiding catalyst damage.[17,18] This setup is often used with higher-temperature plasmas, such as (rotating) gliding arc ((R)GA) or microwave (MW) reactors, where excess plasma heat activates thermal catalysts. Unlike IPC, where the effects of plasma on catalyst and vice versa are vast and go beyond the conventional catalytic paradigm,[16,17] PPC provides a direct link to thermal catalysis, leveraging extensive knowledge from this field. PPC has been explored in various reactor setups and reactions, including NH_3 cracking, CO_2 splitting, CH_4 pyrolysis, and dry, bi- or oxidative reforming of CH_4.[19–22]

PPC-DRM research has spanned multiple reactor designs.[23–29] Allah and Whitehead[25] improved the CO_2 and CH_4 conversion using a planar GA reactor with a NiO/Al_2O_3 catalyst bed. Li *et al.*[21] employed a rotating GA (RGA) reactor with dual CH_4 injection and a $Ni/CeO_2/Al_2O_3$ catalyst, achieving an H_2/CO ratio of 1, which is higher than most reports, but still below the ideal ratio for methanol or dimethyl ether synthesis.[30] Their setup maintained the catalyst bed at 850 °C by encapsulating the reactor exhaust in a tubular furnace, which inherently introduces extra energy costs as an external heat source. Martin-del-Campo *et al.*[28] investigated Ni (15–30 wt%) on Al_2O_3 and SiO_2 supports in an RGA reactor with a spouted catalyst bed, which improved heat transfer. However, the presence of a catalyst in the discharge zone reduced the conversion due to disruption of the arc. In this regard, the authors found that a more stable discharge was achieved with the Al_2O_3-supported catalyst, and that the introduction of catalysts reduced the formation of soot and coke.

Xu *et al.*[29] recently tested a Ni/LDH catalyst diluted with Al_2O_3 beads downstream from a gliding arc plasmatron (GAP) reactor. By heavily diluting the CO_2/CH_4 feed with N_2 (~80%), they achieved equimolar conversion without carbon deposition (*i.e.*, soot/coke). A comparison between a tray-like catalyst bed and a tubular catalyst bed revealed much improved conversion of both CO_2 and CH_4 in the tubular catalyst bed, which the authors attribute to a higher bed temperature. They reported an energy cost (EC) of 4.3 kJ L^{-1}, which was the lowest compared to several other works of literature, albeit this value accounted only for the effective conversion of CO_2 rather than the total conversion (see the discussion below, in Section 3.3.1, for details).

Evidently, studies have demonstrated that placing a Ni-based catalyst bed after the plasma zone improves CH_4 and CO_2 conversion by ensuring unreacted feed gases undergo further catalytic conversion. Additionally, optimizing the position of the Ni/Al_2O_3 spheres after the plasma reactor can enhance heat transfer, reducing the need for external heating. This integration aligns with the goal of developing a fully electrically-driven DRM process, where plasma not only activates reactants but also preheats the catalyst, creating a self-sustaining reaction environment. To overcome the limitations of both standalone plasma and thermal catalysis, rationally designed structured catalysts play a crucial role in bridging the gap between these two approaches, paving the way for a more efficient and scalable DRM technology.

In this study, we implement a Ni/Al_2O_3 catalyst downstream from a GAP plasma reactor. The developed catalyst is first screened and characterised using thermal DRM to determine the optimum Ni loading. Following this, the selected catalyst is introduced into a specially designed post-plasma insulated bed, previously developed in our group for post-CO_2 plasma carbon beds, where we achieved a homogeneous bed temperature without external heating.[31] Importantly, unlike prior studies,[23,24,28,29] our plasma experiments use a pure CO_2/CH_4 mixture (without N_2 or noble gas dilution), reducing costs associated with gas separation and bringing the process closer to industrial relevance.

2. Experimental

2.1. Catalyst preparation

Commercial Al_2O_3 spheres (Sasol, S_{BET} = 200 m^2 g^{-1} and ϕ = 1 mm) were used as the support material for a series of Ni-based catalysts. The diameter was selected to reduce the

pressure drop across the catalyst bed. $Ni(NO_3)_2{\cdot}6H_2O$ (Sigma Aldrich, 99%) was used as Ni precursor in aqueous solution. Different Ni loadings of 2–16 wt% were prepared using incipient wetness impregnation. The samples were henceforth named according to the Ni loading, *i.e.*, 2NiAl (2 wt% Ni), 4NiAl (4 wt% Ni), 8NiAl (8 wt% Ni) and 16NiAl (16 wt% Ni). The impregnated samples were dried overnight and calcined at 800 °C for 2 h under air to form the $NiAl_2O_4$ phase. For the plasma-assisted DRM tests, 100 g of 4NiAl were prepared and activated *ex situ* using a H_2/N_2 (50/50) flow of 100 mL min^{-1} at 750 °C for 3 h before testing.

2.2. Catalyst characterization

X-ray powder diffraction (XRPD) was performed at room temperature over a 2θ range of 4°–100° using a PANalytical X'Pert PRO MPD diffractometer with Cu K_α radiation (λ = 1.5406 Å). Phase identification was conducted by comparing diffraction patterns with the ICDD Powder Diffraction database. Ni content was quantified using a Niton XL3t-Goldd XRF Analyzer (Thermo Scientific). X-ray photoelectron spectroscopy (XPS) measurements were carried out at 5×10^{-10} mbar using a SPECS PHOIBOS 150 hemispherical analyser (SPECS GmbH, Berlin, Germany) with monochromatic Al Kα radiation (1486.74 eV) at 300 W. Spectra were calibrated using the C 1s peak as reference.

N_2 adsorption–desorption isotherms were measured at −196 °C using an Autosorb iQ2 MP instrument. Prior to testing, the samples were degassed at 200 °C for 16 h to remove adsorbed water. The specific surface area (S_{BET}) was determined using multi-point Brunauer–Emmett–Teller (BET) analysis, while pore size distribution was calculated *via* the Barrett–Joyner–Halenda (BJH) method. Hg intrusion porosimetry was conducted with a Thermo-Finnigan porosimeter, from vacuum to 0.2 MPa, followed by measurements between 1 and 200 MPa. Morphological homogeneity and infill patterns of printed structures were analysed *via* optical microscopy (OM), using a Zeiss Discovery V12 stereomicroscope. Scanning electron microscopy (SEM), cross-section analysis, and energy dispersive X-ray (EDX) mappings were performed on a FEI Nova NanoSEM 450 (up to 20 keV) equipped with a Bruker QUANTAX 200 EDX system and XFlash 6160 SDD detector. Cross-section SEM samples were cut at the midpoint and embedded under vacuum in epoxy resin (EpoFix Resin/Hardener).

H_2-temperature programmed reduction (H_2-TPR) was conducted using a micromeritics 3Flex system. Samples were pretreated at 90 °C under Ar, cooled to room temperature, then exposed to a H_2/Ar (10% v/v) flow while heating to 1000 °C at 10 °C min^{-1}. The TCD signal was recorded during reduction. Thermogravimetric analysis (TGA) was performed on a NETZSCH STA449 F3 Jupiter instrument, where 100 mg of sample was heated from 40 to 1000 °C (10 °C min^{-1}) under air flow.

2.3. Thermal catalytic DRM setup

Preliminary thermal DRM tests were conducted in a quartz tube fixed-bed reactor (i.d. = 1.1 cm) placed inside a Carbolite® furnace and connected to a gas chromatograph (Trace 1300 GC, Thermo Fisher Scientific) equipped with two TCDs and one FID detector. A 0.75 g sample of Ni/Al_2O_3 spheres was positioned at the reactor centre, with a thermocouple in direct contact. Prior to catalytic testing, *in situ* pretreatment was performed under a 100 mL min^{-1} flow rate of H_2/N_2 (1/1 molar ratio) at 750 °C for 1 h. The temperature was then reduced to 500 °C under the same gas flow rate. The sample was subsequently exposed to a reactant gas mixture of $CO_2/CH_4/N_2$ (1/1/3) at a total inlet flow rate of 100 mL min^{-1}, corresponding to a gas hourly space velocity (GHSV) of 8000 mL g_{cat}^{-1} h^{-1}. The catalytic performance was evaluated over a temperature range of 500–800 °C at 0.1 MPa. A long-term catalytic test (5 days) was conducted for the most efficient catalysts at 700 °C, using again 0.75 g of catalyst, 0.1 MPa, and the same GHSV of 8000 mL g_{cat}^{-1} h^{-1} with the same reactant gas mixture ($CO_2/CH_4/N_2$ = 1/1/3). After the tests, samples were thoroughly characterized, and product analysis was performed online using a gas chromatograph. CO and H_2 were the main observed products, with trace amounts of C_2H_4 and C_2H_6 detected.

2.4. Plasma-catalytic DRM setup

Post-plasma catalysis tests were conducted using a gliding arc plasmatron (GAP) reactor, as described in previous studies.[29,32,33] The Ni-based catalyst (4NiAl) was loaded into a bed attached to the outlet of the GAP reactor, with 8 g used in each experiment. The bed design forces the high-temperature effluent from the plasma reactor through the catalyst and around the bed in an insulating manner (see ESI,† Fig. S1a), thus ensuring better heat retention and a more consistent bed temperature throughout the whole volume. The extended anode ensures the catalyst is positioned sufficiently far from the plasma to avoid direct contact with it and thus thermal-associated catalyst damage. In addition, this bed feature reduces the likelihood of plasma-generated reactive species (*i.e.*, radicals/ions) from reaching the catalyst, as the lifetime of such species at atmospheric pressure is short. Therefore, the plasma effect is solely to thermally activate the catalyst. Benchmark tests were performed with an empty catalyst bed. A schematic of the reactor setup with the insulated catalyst bed is shown in Fig. S1b (ESI†). Each experiment was run in triplicate for 1 h. Additionally, one long run of 6 h was conducted using the 30 vol% CH_4 fraction, to demonstrate the capability of the system for extended coupled plasma-catalytic performance.

CO_2 and CH_4 (99.999% and 99.995%, Air Liquide) were supplied to a single gas inlet connected to a swirl ring containing six tangential inlets, and the flow rate was controlled using mass flow controllers (MFCs) (Bronkhorst, F-201AV/F-201CV). The unit of flow rate was set according to the Bronkhorst standard litre per minute, which aligns with the standard EU definition taken at 20 °C and 0.1 MPa (molar volume = 24.06 L mol^{-1}). The total flow rate was set to 10 L min^{-1}, while the CO_2/CH_4 ratio was varied from 90/10 vol% to 50/50 vol%. The GHSV was fixed at 75 000 mL g_{cat}^{-1} h^{-1}. In all post-plasma catalysis tests, no diluting gas was present. The inlet pressure was monitored throughout with a pressure gauge, with the average readings shown in ESI† (Table S1). The maximum recorded pressure difference between the benchmark and plasma-catalytic experiments was approximately 0.2 bar. The outlet

gas mixture was analysed using non-dispersive infrared (NDIR) detectors for CO, CO_2, and CH_4, along with a thermal conductivity detector (TCD) for H_2 (Emerson, XSTREAM XEGP Continuous Gas Analyser). We specifically note that the total concentration of all four measured gases (CO, CO_2, CH_4 and H_2) amounted to 100.0 ± 1.5 vol%. This suggests that other gaseous products, *e.g.* saturated and unsaturated hydrocarbons, may have been formed but not in significant amounts (which would have led to larger total concentration deviation from 100 vol%) and were thus neglected. To condense liquid products and remove solid particles, a cold trap, in-line filters, and a lab-scale cyclone separator were installed between the reactor and analytical equipment (see Fig. S1b, ESI†). Spatial temperature measurements were obtained at four distinct locations post-plasma, using a digital thermometer (Omega, HH520) with K-type thermocouples inserted into the exhaust chamber. The first thermocouple (T1 in Fig. S1b, ESI†) was inserted into the catalyst bed, providing insights into the average gas temperature within the bed. The following three thermocouples (T2–4 in Fig. S1b, ESI†) measure the effluent temperature in the greater reactor exhaust (*i.e.*, not within the catalyst bed). The negative polarity current-controlled power supply unit (PSU) was connected to the high-voltage electrode while the reactor body was grounded. The current was fixed between 650 and 690 mA, with the exact value depending on the current required to sustain a stable discharge (Table S2, ESI†). The working voltage was free to vary according to the plasma length and resistivity (typically 1.30–1.55 kV). The voltage differential across the plasma was measured using a high-voltage probe (Tektronix, P6015A) connected across the reactor and recorded using a digital oscilloscope (Keysight, DSOX1102A). In addition, a current sense resistor (2 Ohm) was connected to measure the current through the plasma. Two ballast resistors (1000 Ohm) were placed in series between the PSU and reactor to increase the resistive load detected by the PSU, resulting in a more stable discharge. The plasma typically exists in a takeover mode,[34,35] manifested as quasi-periodic peaks in current and voltage. We specifically note that the measured power is the plasma-deposited power, thus the power losses in the PSU and circuit (*e.g.*, in ballast resistors) is not included. This is common practice in plasma-based literature and enables a more fair comparison between studies.

Reactor performance was assessed using formulae previously defined by Wanten *et al.*[36] This study evaluates performance in terms of absolute, effective, and total conversion. To quantify the energy performance, we define the EC of the process in relation to the total conversion. It is important to use the total conversion in this calculation for multi-component mixtures, where more than one reactant is being converted (as is the case with DRM). All formulae, including the flux ratio considerations (accounting for gas expansion, inherent to DRM), are provided in the ESI,† section S1.

3. Results and discussions

3.1. Catalyst characterization

Four $NiAl_2O_4$ samples with Ni loadings of 2, 4, 8, and 16 wt% were prepared and labelled as 2NiAl, 4NiAl, 8NiAl, and 16NiAl, respectively. The final Ni loadings were close to the target values (Table 1). XRD patterns revealed peaks corresponding to the $NiAl_2O_4$ phase, which shifted to lower angles upon increasing Ni content, indicating Ni incorporation into the Al_2O_3 lattice structure (Fig. 1a). The NiO phase was not detected, suggesting its presence was negligible. An activation treatment was necessary to generate Ni nanoparticles from $NiAl_2O_4$ before DRM tests, enabling controlled Ni segregation to the surface.[37,38] For the characterization of the activated NiAl samples (NiAl-act), the samples were reduced *ex situ* at 750 °C and analysed by XRD (Fig. S2, ESI†). After reduction, small metallic Ni (Ni°) peaks at 2θ = 44.5, 51.8 and 76.4° were observed for 4NiAl-act, 8NiAl-act, and 16NiAl-act, with crystallite sizes varying by Ni loading (Table 1). In contrast, no Ni° peaks were detected for 2NiAl-act, suggesting the presence of Ni clusters (Fig. S2, ESI†). The samples displayed mesoporosity (Fig. S3, ESI†), with a slight decrease in S_{BET} surface area and pore volume (V_p) compared to pristine Al_2O_3 support, attributed to Ni incorporation. As such, the S_{BET} and V_p was reduced upon increasing Ni loading (Table 1). Activation treatment (*e.g.*, for 4NiAl and 16NiAl) had minimal impact on their mesoporosity (Fig. S4, ESI†), indicating the preservation of textural properties. H_2-TPR experiments showed H_2 consumption starting at 750 °C, corresponding to NiO reduction within $NiAl_2O_4$ to metallic Ni, shifting to higher temperatures upon decreasing Ni concentration (Fig. 1b).[37–39] This trend indicates stronger interactions between smaller Ni nanoparticles and the support, reflected in slightly increasing normalized H_2 consumption values upon decreasing Ni loading (Table 1).

Optical microscopy (OM) of 4NiAl, selected for deeper characterization due to its high thermal DRM performance and moderate carbon formation (Fig. 2 and Fig. 3, discussed later), showed a homogeneous particle size distribution (~1.0 mm, Fig. 1c). Cross-sectional SEM images confirmed the predominance of mesoporosity (d_p < 50 nm) (Fig. 1d and e). This was further validated by Hg intrusion porosimetry (Fig. S5, ESI†), which revealed a minimal presence of macropores. EDX mapping demonstrated homogeneous Ni dispersion within the $NiAl_2O_4$ spinel (Fig. 1e). Cross-sectional SEM and EDX analyses of reduced 4NiAl sample (4NiAl-act) showed no significant structural differences compared to 4NiAl (Fig. S6, ESI†). Hg intrusion porosimetry also confirmed that activation at 750 °C did not significantly alter the porosity (Fig. S5, ESI†), indicating the preservation of textural properties.

Table 1 Characteristics of the NiAl samples

	Ni content (wt%)	Crystallite size of Ni^0 by XRD[a] (nm)	S_{BET} ($m^2\ g^{-1}$)	V_p ($cm^3\ g^{-1}$)	H_2 consumption[b] (mol H_2 mol_{Ni}^{-1})
Al_2O_3	—	—	200	0.52	—
2NiAl	2.1	—	160	0.47	1.56
4NiAl	4.3	9	156	0.45	1.49
8NiAl	8.1	13	146	0.42	1.48
16NiAl	15.9	19	130	0.37	1.47

[a] After activation treatment. Treatment conditions:100 mL min^{-1}; H_2/N_2 = 1/1; T = 750 °C. [b] From H_2-TPR experiments.

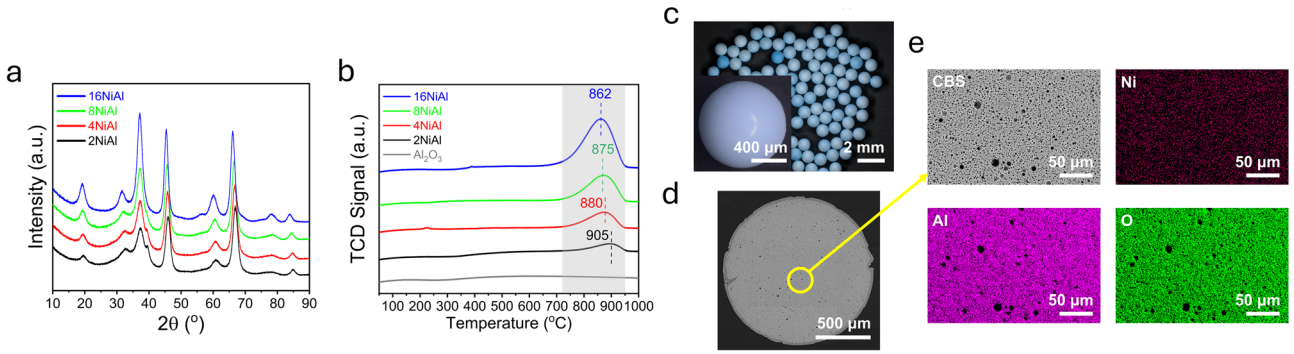

Fig. 1 Characterization of NiAl samples. (a) XRD patterns and (b) H_2-TPR of NiAl samples. (c)–(e) Textural characterization of 4NiAl: (c) OM, (d) cross-sectional SEM images and (e) EDX mapping.

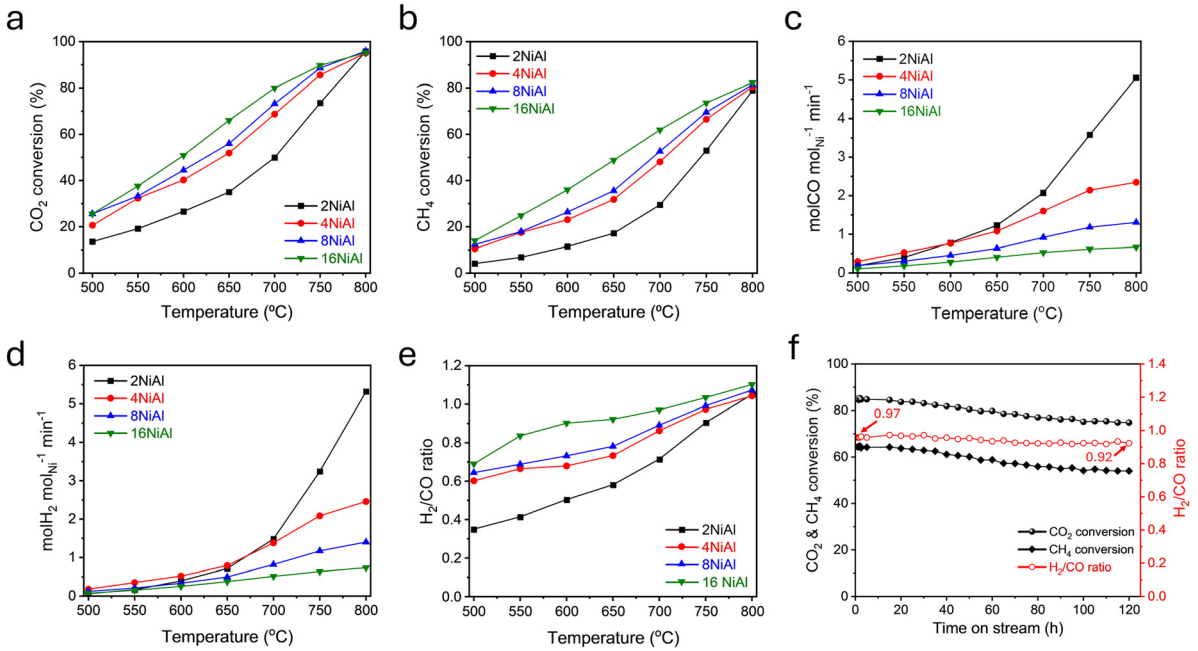

Fig. 2 Catalytic behaviour of the NiAl samples in the thermal DRM. (a) CO_2 conversion, (b) CH_4 conversion, (c) CO production, (d) H_2 production, and (e) H_2/CO molar ratio, for the four different NiAl samples, and (f) stability test of the 4NiAl sample at 700 °C. Reaction conditions: pressure = 0.1 MPa, CO_2/CH_4/N_2 = 1/1/3, GHSV = 8000 mL g_{cat}^{-1} h^{-1}, m_{cat} = 0.75 g. Pre-treatment conditions: pressure = 0.1 MPa, H_2/N_2 = 1/1, T = 750 °C.

XPS analysis of 4NiAl revealed a feature corresponding to Ni^{2+} in $NiAl_2O_4$ within the Ni $2p_{3/2}$ core level spectrum (Fig. 3a).[40] After activation (4NiAl-act), a shift to lower binding energy suggested Ni° formation on the surface.[41] The slightly higher binding energy of Ni° compared to reported values indicated strong Ni-support interactions, aligning with the H_2-TPR results.[38,39] No differences were observed in the C 1s core level spectrum (Fig. 3b).

3.2. Thermal catalytic DRM tests

Thermal catalytic tests showed that all NiAl samples, prior to activation, were active under the reaction conditions. CO_2 and CH_4 conversion increased with temperature, reaching equilibrium conversion values at 800 °C (95% and 82%, respectively) for all samples (Fig. 2a and b). Among them, 16NiAl exhibited the highest performance per mass of catalyst loading (Fig. S7, ESI†). However, when syngas production (CO + H_2) was normalized to Ni loading (Fig. 2c and d), 2NiAl displayed the highest catalytic activity, attributed to its smaller Ni crystallites and greater Ni surface exposure.

The syngas ratio (H_2/CO) increased with both temperature and Ni loading, exceeding 1.0 for all samples at 800 °C (Fig. 2e). This suggests that higher Ni loadings enhance CH_4 decomposition, which benefits H_2 production, but also having the drawback of accelerated carbon formation. For stability testing at 700 °C over 120 h, 4NiAl was selected due to its higher catalytic activity compared to 2NiAl and lower coke formation than 8NiAl and 16NiAl (Fig. S7 (ESI†) and Fig. 3c). The large coke formation leads to catalyst deactivation and increased reactor pressure drop. The stability test showed a slight deactivation after 120 h,

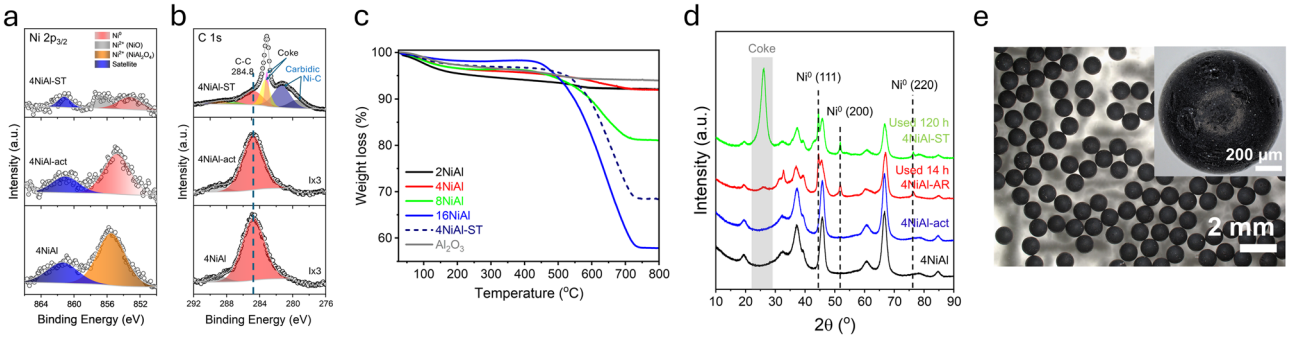

Fig. 3 Characterization of used NiAl catalysts. (a) Ni 2p3/2 and (b) C 1s XPS spectra of fresh (4NiAl), activated (4NiAl-act) and used samples after stability test at 700 °C (4NiAl-ST). (c) TGA of used NiAl samples under air. (d) XRD patterns of 4NiA, 4NiAl-act, 4NiAl-AR (14 h under reaction at T = 500–800 °C) and 4NiAl-ST (120 h under reaction at 700 °C). (e) OM images of 4NiAl-ST.

with the conversion value decreasing *ca.* 11%, from 85% to 74%. As the drop in CO_2 conversion was a bit less than that in CH_4 conversion, the syngas ratio slightly decreased from 0.97 at 1 h to 0.92 at 120 h (Fig. 2e). This suggests that coke formation deactivated some active sites, without significantly triggering secondary reactions like the reverse water–gas shift (RWGS) or CH_4 decomposition.

Post-reaction characterization included TGA analysis of used NiAl samples after 14 h of screening tests (500–800 °C) in air, showing weight loss from coke oxidation (Fig. 3c). The 4NiAl sample after the 120 h stability test at 700 °C (4NiAl-ST) exhibited lower weight loss than 16NiAl, despite the latter undergoing only 14 h of reaction (Fig. 3c). This highlights the importance of optimizing catalyst composition to enhance long-term performance, while minimizing deactivation and solid carbon (*i.e.*, coke/soot) accumulation, which could cause increased reactor pressure drops.

XPS analysis of 4NiAl after the stability test (4NiAl-ST) revealed Ni $2p_{3/2}$ peaks corresponding to Ni^{2+} (NiO) and metallic Ni (Fig. 3a and b). The Ni° peak in 4NiAl-ST was shifted to a lower binding energy (BE) compared to 4NiAl-act, suggesting weaker Ni-support interactions (Fig. 3a), and the formation of larger Ni nanoparticles. XRD analysis confirmed this, showing Ni° nanoparticle sintering in used 4NiAl samples (4NiAl-AR (*i.e.*, after reaction of 14 h): 15 nm and 4NiAl-ST: 18 nm), with no crystalline NiO detected (Fig. 3d).

The C 1s XPS spectrum of 4NiAl-ST showed a high-intensity peak at 283.0 eV and 283.4 eV, indicating different types of coke (Fig. 3b).[39] Additionally, a lower BE feature suggests carbidic carbon (Ni–C).[39,42,43] XRD patterns of 4NiAl-ST supported the formation of solid carbon (coke), showing a broad peak at $2\theta = 26°$ (Fig. 3d). The presence of solid carbon was also visually evident from the coloration of the sample after the reaction (Fig. 3e). Solid carbon deposition reduced the S_{BET} surface area and pore volume of 4NiAl after the stability test, with values decreasing from 156 to 116 $m^2\ g^{-1}$ for S_{BET} and 0.45 to 0.32 $cm^3\ g^{-1}$ for V_p, respectively (Fig. S8, ESI†). Hg intrusion porosimetry of 4NiAl-ST further confirmed pore blockage, as indicated by a decrease in total pore volume (Fig. S5, ESI†).

3.3. Plasma-catalytic DRM tests

3.3.1. Conversion. To boost both the conversion and production rates of plasma-based DRM, a Ni catalyst (4NiAl) with the demonstrated thermo-catalytic activity was implemented downstream from the plasma reactor. The absolute conversion of CO_2 and CH_4 as a function of CH_4 fraction at the inlet are shown in Fig. 4a, both in the absence and presence of said catalyst.

At low CH_4 fractions (*i.e.* 10 and 20 vol%), the presence of a catalyst has a small negative effect on the CO_2 conversion, *i.e.*, *ca.* 2% reduction in conversion. This reduction is likely due to

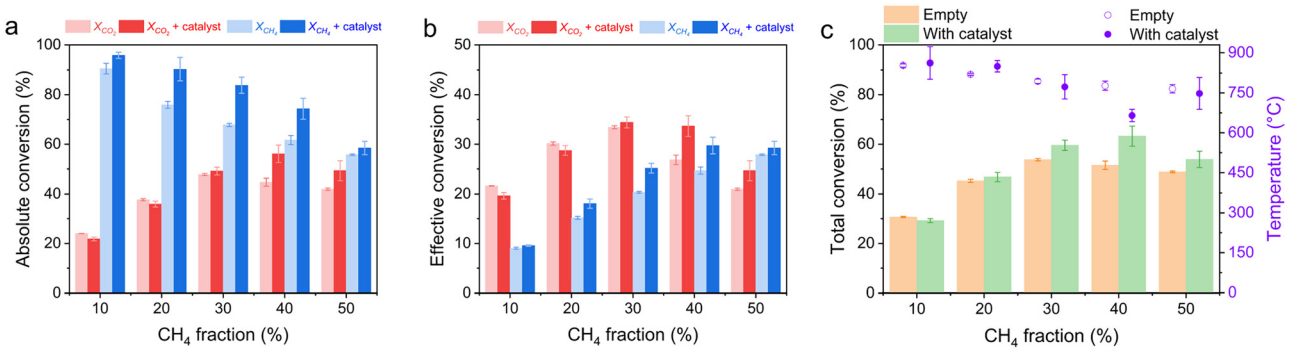

Fig. 4 Performance of the post-plasma-catalytic DRM reaction using 4NiAl-act sample. (a) Absolute conversion of CO_2 and CH_4 with and without catalyst, (b) effective conversion of CO_2 and CH_4 with and without catalyst, and (c) total conversion of CO_2 and CH_4 with and without catalyst. The 4NiAl sample was *ex situ* activated (H_2/N_2 = 1/1, T = 750 °C) prior to testing.

an enhanced water gas shift (WGS) reaction, in which CO and H_2O react to form CO_2 and H_2. The forward reaction proceeds instead of the reverse (RWGS) reaction due to insufficient H_2. As the CH_4 fraction increases, the proportion of H_2O formed decreases. As this occurs, the rate of the WGS reaction also decreases, resulting in a small rise in CO_2 conversion at 30 vol% CH_4 inlet fraction (+2%). At the highest examined CH_4 fractions (40 and 50 vol%), solid carbon deposition from the CH_4 decomposition becomes more prevalent. While this is detrimental for the catalyst activity and leads to deactivation, the produced solid carbon can react with the gas phase CO_2 *via* the reverse Boudouard reaction to increase the CO_2 conversion.[31,44,45] As a result, the optimum CO_2 conversion in the presence of a catalyst is achieved with 40 vol% CH_4 at the inlet (+10% rise compared to without catalyst).

For the CH_4 conversion, the presence of the catalyst improves the performance for all examined CH_4 fractions. Upon increasing CH_4 fraction at the inlet, the absolute conversion decreases from a maximum value around 96% (10 vol% CH_4, with catalyst) to 59% (50 vol% CH_4, with catalyst). The largest proportional increase upon adding the catalyst is observed with 30 vol% CH_4 fraction at the inlet, with the conversion increasing by approximately 24% (from 68% to 84%). The lower effectiveness of the catalyst at higher CH_4 fractions (40 and 50 vol%) is likely due to coke deposition and the resulting catalyst deactivation, as also observed in the thermal DRM (Fig. 2 and 3).

Direct comparison to the conversions obtained by thermal-catalytic testing is not possible due to the presence of a diluting gas in the thermal cases (N_2), which was needed to limit solid carbon production and thus enable longer experiments. However, we can contrast the absolute conversions realised with 50 vol% CH_4 in the PPC case to those obtained in the thermal-catalytic tests for 4NiAl around 700 °C (Fig. 4a and b). Interestingly, the CO_2 conversion is lower while the CH_4 conversion is higher in the PPC scenario. This difference likely arises due to the fact that conversion occurs in the plasma reactor prior to entering the bed, as shown in the empty bed case (Fig. 4a). This pre-bed conversion effect coupled with the dilution required in the thermal-catalytic experiments serves to highlight the fact that direct comparison between the thermal and PPC experiments is not applicable, and that the results obtained in the thermal-catalytic case are simply indicators of a potential coupling. Replicating the plasma effluent mixture obtained from pre-bed reactant conversions and their effect on the thermal-catalytic conversion would be an interesting avenue of study, but is outside the scope of this work.

While high absolute reactant conversions can be obtained, especially highlighted by the near complete CH_4 conversion with catalyst at 10 vol% CH_4 (Fig. 4a), the effective conversion is a more relevant metric to account for the proportion of inlet stream that contains the reactant of interest (eqn (S8), ESI†). Thus, the effective conversion of CO_2 and CH_4 in the presence and absence of catalyst as a function of CH_4 inlet fraction is shown in Fig. 4b. At a single inlet fraction, the absence or presence of a catalyst follows the same trend as the absolute conversion for both CO_2 and CH_4. The effective CO_2 conversion peaks around 30 to 40 vol%, reaching a maximum value around 34%. Contrary to the absolute CH_4 conversion trend, the effective conversion increases as a function of increasing CH_4 inlet fraction, peaking around 30% for the inlet fractions of 40 and 50 vol%.

The absolute conversion values achieved in this work are lower than those reported by Xu *et al.*,[29] especially when compared at the same molar ratio of CO_2/CH_4 (*i.e.* 1/1 or 50 vol% CH_4). However, we used a non-dilute CO_2/CH_4 stream as the feed gas, whereas Xu *et al.*[29] utilised an inlet stream of only 10 vol% CO_2 and 10 vol% CH_4, heavily diluted with N_2 (80 vol%).

The authors did so to facilitate plasma ignition and sustainment at this ratio, while minimizing coke deposition, and it was reported several times that N_2 enhances the (absolute) CO_2 and CH_4 conversion.[46–49] Hence, we advocate that the effective conversion is a more comparable metric, as it accounts for the proportion of reactant converted with regards to the amount supplied at the inlet. The corresponding best effective CO_2 and CH_4 conversion values achieved by Xu *et al.* were 7 and 9%, respectively (Table 2). When compared to the effective conversion obtained with our setup (Fig. 4b), all examined conditions in our study demonstrate an improvement. The highest effective CO_2 conversion is achieved at both 30 and 40 vol% CH_4 at the inlet, reaching a value around 34%. The peak effective CH_4 conversion is achieved at 40 vol% CH_4, reaching 30%. The five-fold increase in effective CO_2 conversion and three-fold increase in effective CH_4 conversion demonstrate the detrimental effect of dilution on the performance. In addition to reducing the effective conversion values, the cost and complexity of separating the effluent mixture also increases with dilution, making the process less appealing for scaled-up applications, and therefore for cost-effective industrial processes.

Other than effective conversion, the total conversion can also be used to provide a more global view of the process performance.[36] As this is a summation of the effective conversion values (eqn (S9), ESI†), the effect of dilution is also considered. Xu *et al.* obtained a peak total conversion of *ca.* 16%,[28] whereas we obtained values up to 63% (at 40 vol% CH_4 inlet fraction), which is nearly four times higher (Fig. 4c). In addition, the temperature measured inside the post-plasma catalyst bed (T1) is shown in Fig. 4c, with all four thermocouple readings shown in Fig. 5 (T1–T4, see setup schematic in Fig. S1b, ESI†). For both empty and filled cases, the increasing CH_4 fraction in the inlet feed resulted in a lower temperature in the bed and reactor exhaust. This correlates with previous observations in literature[33,50] and is associated with the changes to the mixture thermal conductivity and heat capacity.[50] As demonstrated by the CO_2 and CH_4 conversion shown in the thermal catalytic tests (Fig. 2a and b), the optimum catalyst temperature is around 800 °C. In the PPC cases, 10% CH_4 at the inlet slightly overshoots this ideal temperature, reaching bed temperatures around 900 °C, while 30–50% CH_4 inlet concentrations slightly undershoot the optimum temperature (bed temperature *ca.* 700 °C). Only with 20

Table 2 Overview of post-plasma-catalytic DRM literature

Reactor type	Catalyst	Diluting gas	$CO_2:CH_4$	Total flow (L min^{-1})	Power (kW)	Absolute conversion (%)		Effective conversion (%)		(MJ mol^{-1} reactants)	Ref.
						CO_2	CH_4	CO_2	CH_4		
Glow discharge	—	—	3 : 1	1		55	85	41	21	0.34	51
Rotating gliding arc	—	70% Ar	1 : 1	3.7	0.16	10.9	12.8	1.6	1.9	4.6	52
Microwave	—	—	1 : 1	30	6	70	96	35	48	0.35	53
Thermal arc	Ni/Al_2O_3	77% N_2	3 : 2	36.7	9.6	88	76	10.5	7	89.8	23
Thermal arc	Ni/Al_2O_3	16% Ar 27% N_2	3 : 2	117	14.4	77	62.4	29.2	15.8	16.4	24
Planar gliding arc	NiO/Al_2O_3	—	1 : 1	2.5	0.15	19	17	9.5	8.5	20	25
Rotating gliding arc	$Ni/CeO_2/Al_2O_3$	—	7 : 3	6	0.49	39.5	58.5	11.9	41	9.3	26
Rotating gliding arc	Ni/Al_2O_3	—	1 : 1	2.7	0.49	91	94	45.5	47	12	27
Rotating gliding arc	$Ni/CeO_2/Al_2O_3$	70% Ar	3 : 2	3.7	0.14	10.9	11.8	2	1.4	65.3	28
Gliding arc plasmatron	Ni/LDH	80% N_2	1 : 1	8	0.51	79	91	7.9	9.1	0.52	29
Gliding arc plasmatron	Ni/Al_2O_3	—	3 : 2	10	1.05	56	74	33	29	0.24	This work

vol% CH_4 prescribed at the inlet reaches the ideal bed temperature (*ca.* 800 °C) at the applied current. The conversion realised at 10 vol% CH_4 and 30–50 vol% CH_4 could be improved by either reducing or increasing the catalyst bed temperature respectively, which is achieved by decreasing or elevating the SEI at these conditions. This can be achieved either by power or flow rate regulation, with the former being achieved by current modulation. Nevertheless, in general, all conditions yield catalyst bed temperatures in the range of optimal performance determined by the thermal-catalytic testing. For all examined cases, the temperature decreases as the gas travels through the plasma reactor exhaust (*i.e.*, from T2 to T4). This occurs due to the conductive heat losses through the stainless steel exhaust walls.

3.3.2. Production rates and syngas ratio. The production rates of both CO and H_2 per mole of Ni loading as a function of CH_4 fraction supplied at the inlet are shown in Fig. 6a.

When rising the inlet fraction from 10 to 40 vol% CH_4, both CO and H_2 production rates increase. The CO rate increases from 10.7 molCO mol_{Ni}^{-1} min^{-1} at 10 vol% CH_4 to a peak value of *ca.* 24.3 molCO mol_{Ni}^{-1} min^{-1} at 40 vol% CH_4. Concurrently, the H_2 production rate increases from 4.1 molH$_2$ mol_{Ni}^{-1} min^{-1} to a near-equal peak value of 24.4 molH$_2$ mol_{Ni}^{-1} min^{-1} at the same data points. Interestingly, at 50 vol% CH_4, the molar CO production rate decreases to *ca.* 19.6 molCO mol_{Ni}^{-1} min^{-1}. This drop can be attributed to the lower CO_2 concentration in the inlet, which acts as the limiting reactant for CO production. At the same inlet CH_4 fraction, the H_2 production rate remains relatively constant (*ca.* 24.5 molH$_2$ mol_{Ni}^{-1} min^{-1}) despite a drop in absolute conversion. This is due to the CH_4 decomposition, which remains constant at this CH_4 concentration. This levelling occurs as the drop in volumetric flow rate at the exhaust (observed with increasing fraction of CH_4 at the inlet due to solid carbon formation) is proportional to the drop in the outlet CO concentration (see eqn (S10), ESI†).

In comparison to the production rates realised in the thermo-catalytic tests (Fig. 2c and d), both CO and H_2 production rates are significantly increased in our post-plasma catalysis experiments. These trends are logical, as the GHSV increases by an order of magnitude between the experimental setups. The CO production rate is enhanced almost five-fold for the lowest plasma-based case (from 2.4 to 10.7 molCO mol_{Ni}^{-1} min^{-1}), a value which is more than doubled to 24.3 molCO mol_{Ni}^{-1} min^{-1} at the highest CO production rate (at 40 vol% CH_4 inlet fraction), leading to ten times higher CO production rate in post-plasma catalysis *vs.* thermal catalysis. The H_2 production rate is similarly enhanced. Although the enhancement is less than two-fold in the lowest case (10% CH_4 inlet fraction) from 2.5 to 4.1 molH$_2$ mol_{Ni}^{-1} min^{-1}, it elevates rapidly with increasing inlet CH_4 fraction, resulting in a peak value increasing again ten-fold when compared to the best result in thermal catalysis (from 2.5 to 24.5 molH$_2$ mol_{Ni}^{-1} min^{-1}). The dramatic increase in production rates in the PPC experiments

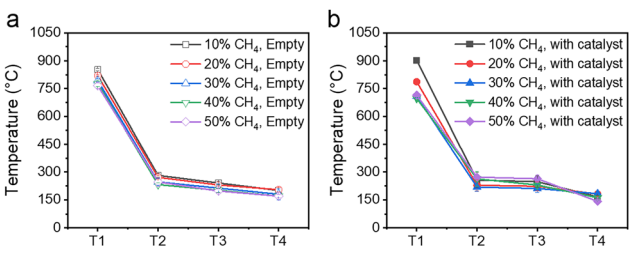

Fig. 5 Average temperature with (a) empty catalyst and (b) filled catalyst bed with 4NiAl. Recorded at four locations along reactor body (*T1* = inside catalyst bed, *T2* = 10 cm from reactor outlet, *T3* = 20 cm from reactor outlet, *T4* = 30 cm from reactor outlet).

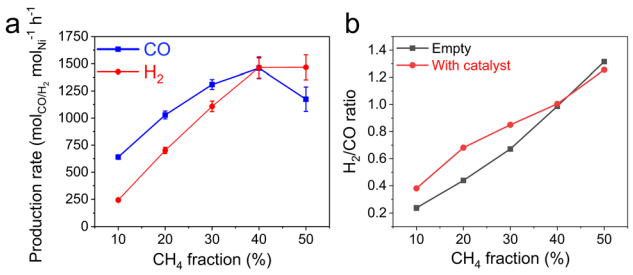

Fig. 6 Performance of the post-plasma-catalytic DRM reaction using 4NiAl-act sample. (a) Molar production rate of CO and H_2 in relation to Ni loading, and (b) syngas ratio (H_2/CO) as a function of increasing CH_4 inlet concentration. The 4NiAl sample was *ex situ* activated (H_2/N_2 = 1/1, *T* = 750 °C) prior to testing.

can be attributed to the high absolute conversion of CO_2 and CH_4 in combination with the higher flow rates (and hence increased GHSV) in the plasma reactor setup. These improvements serve to highlight the potential advantage of implementing an optimised thermal catalyst downstream from a plasma reactor, enhancing both conversion and syngas production rates compared to operating plasma without a catalyst. Indeed, scaling up of the process from a smaller-scale thermal catalysis setup to a larger-scale plasma system is demonstrated by the increased production rates of CO and H_2.

The syngas ratio (H_2/CO) (Fig. 6b) increases with CH_4 fraction, both in the presence and absence of the catalyst. The increased amount of CH_4 at the inlet produces more H_2, which rises faster than the CO production rate (Fig. 6a), explaining the logical trend in Fig. 6b. Additionally, when the catalyst is incorporated downstream, we observe a slightly higher syngas ratio (1.25–1.5 fold) compared to the empty plasma reactor in the range of 10 to 30 vol% CH_4. At 40 vol%, the catalyst presence has no significant effect on the ratio, whereas for 50 vol% we observe a slightly detrimental effect. The explanation for this is two-fold, firstly by the greater carbon deposition from the improved dehydrogenation capability of the Ni catalyst, which promotes CH_4 decomposition. This solid carbon can then be oxidised by the CO_2 *via* the reverse Boudouard reaction, which increases the CO production. Secondly, the conversion of CH_4 is lower at 50 vol% CH_4, and both factors contribute to a lower syngas ratio in the presence of catalyst at this fraction.

3.3.3. Energy cost. The EC realised with our setup for all inlet CH_4 fractions is shown in Fig. 7. The EC remains relatively constant between the empty bed and the bed with the packed catalyst for all inlet CH_4 fractions. We observe the lowest EC at 40 vol% CH_4 at the inlet, reaching around 0.24 MJ mol^{-1} (with or without catalyst). At 50 vol% CH_4 inlet fraction, the EC is slightly higher, reaching 0.28 MJ mol^{-1}, both with and without catalyst present. This can be correlated to the lower total conversion observed at this data point (Fig. 4c).

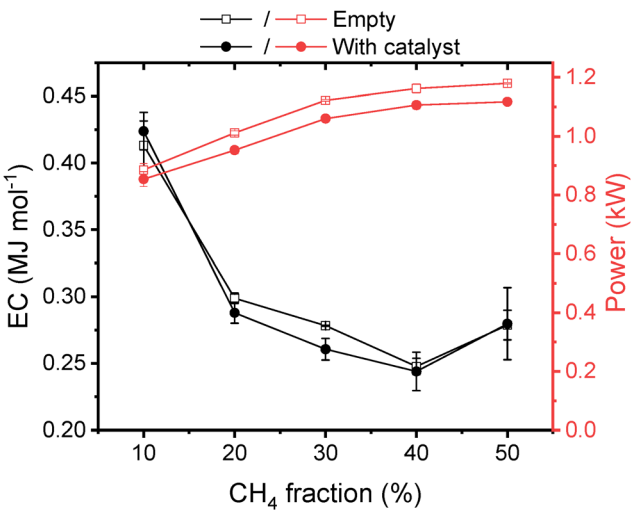

Fig. 7 Performance of the post-plasma-catalytic DRM reaction using 4NiAl-act sample. Energy cost (per mol of reactant mixture) for total conversion as a function of increasing inlet CH_4 fraction. The 4NiAl sample was *ex situ* activated (H_2/N_2 = 1/1, T = 750 °C) prior to testing.

When comparing these results with the EC values obtained by Xu *et al.*,[29] who used a similar reactor setup and catalyst (*i.e.* GAP and Ni-based), we should note that Xu *et al.* reported the EC related exclusively to the effective conversion of CO_2. While this formula can be applied if the focus is on CO_2 conversion, the DRM-oriented research best uses the EC values calculated based on the recommendation of Wanten *et al.*,[36] *i.e.* on the total conversion (eqn (S9), ESI†). As such, the effective conversion of both CO_2 and CH_4 is considered. If the same equation is applied to the results of Xu *et al.*, the authors reached an optimum EC of 0.52 MJ mol^{-1}. Thus, our EC is about a factor two lower for all examined CH_4 inlet fractions, especially at the optimum inlet fractions of 30 and 40 vol% CH_4 (EC = 0.25 MJ mol^{-1}).

Finally, we also compared our results with other data reported in literature for post-plasma-catalytic DRM with various plasma reactors, shown in Table 2. Evidently, several different types of reactors have been investigated, with most implementing a thermal plasma. This is logical, as PPC utilises sensible or waste heat from the plasma reactor to facilitate the catalysis.

For the sake of completeness, we also added a few entries of plasma-based DRM without catalysts. While they are often characterised by lower conversion and higher EC, the examples shown are some of the best results in literature to-date. Nonetheless, the realised ECs are slightly worse than those obtained in this study. However, the latter comes with the cost of adding a catalyst. Overall, a main advantage of post-plasma catalysis is the utilisation of the waste heat from the plasma reactor to heat the catalyst bed, which equates to heat integration. Heat integration could in principle also be performed without catalyst, by using the effluent heat to preheat the inlet gas (so that less power is needed to reach the same level of conversion), but this is not yet commonplace in plasma reactors.

It is clear that the EC realised at the optimum condition in our study is the lowest reported in literature to date, with mostly higher effective CO_2 and CH_4 conversions.

3.3.4. Extended catalytic test. To further establish the viability of post-plasma-catalytic DRM, we conducted a long-run test of 6 h for 30 vol% CH_4 at the inlet, which is shown in Fig. 8. While an inlet CH_4 fraction of 30 vol% did not produce the highest conversion or the lowest EC (see above), this condition yielded significantly less carbon deposition than 40 or 50 vol% CH_4, while also demonstrating the greatest EC improvement when comparing the results with and without catalyst. Hence, this fraction was deemed the most viable for a long-run test.

As seen in Fig. 8, the CO_2 and CH_4 fractions decrease rapidly upon plasma ignition, with the CO_2 decreasing from 70 to *ca.* 25 vol% after 10 min, and CH_4 decreasing from 30 to 4 vol% in the same period. These values continue to decline until about 60 min, after which they remain constant around 22 vol% and 2.5 vol%, respectively, for the remainder of the test. Simultaneously, the CO and H_2 values increase dramatically in the first 10 min, reaching values around 39 and 32 vol%, respectively. These values rise further until about 60 min, reaching again

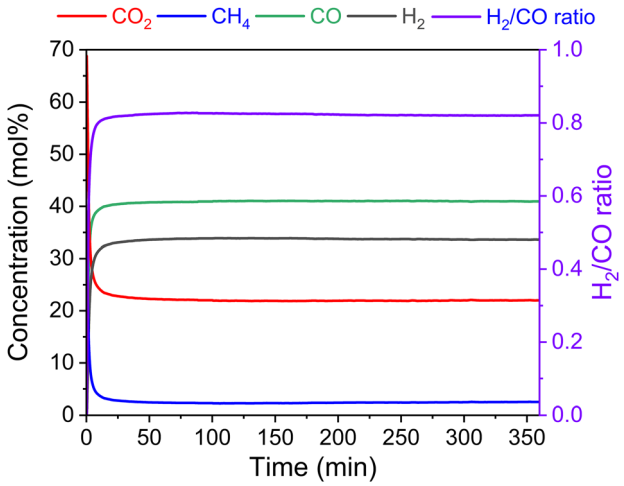

Fig. 8 Performance of the post-plasma-catalytic DRM reaction using 4NiAl-act sample. Real-time reactant and product concentrations and syngas ratio for 30 vol% CH_4 fraction at the inlet for 6 h. The 4NiAl sample was *ex situ* activated (H_2/N_2 = 1/1, T = 750 °C) prior to testing.

steady-state values around 41 and 34 vol%. Since these values remain relatively constant throughout the experiment, the syngas ratio (H_2/CO) also stabilizes at a steady-state value of 0.83. While this timeframe was not necessarily long enough to be considered a formal stability test, the thermal catalysis results align well in this first 6 h period. Thus, it is reasonable to assume that the performance may decline slightly over much longer timescales (>100 h) due to catalyst deactivation from coke deposition, though not significantly (see Fig. 2f).

4. Conclusions

We studied thermal and post-plasma catalysis for DRM using the same Ni/Al_2O_3 catalysts. We first prepared four Ni/Al_2O_3 samples with varying Ni loadings (2, 4, 8, and 16 wt%), characterized and tested them in thermal catalytic DRM. The activation of $NiAl_2O_4$ to produce Ni/Al_2O_3 catalysts did not significantly alter the textural properties of the $NiAl_2O_4$ spheres. The thermal catalytic results and characterization of the used catalysts in thermal DRM showed that the $NiAl_2O_4$ sample with Ni loading of 4 wt% was the most suitable for further study in post-plasma-catalytic DRM. This catalyst exhibited higher activity (per gram of catalyst) than the 2 wt% sample and lower coke formation than the 8 wt% and 16 wt% samples. These two parameters are crucial for maintaining stable catalytic activity and minimizing coke formation, which helps prevent excessive pressure drop in the post-plasma catalyst bed.

The post-plasma-catalytic DRM showed improved CH_4 conversion compared to plasma alone, for all examined inlet CH_4 fractions (10–50 vol%), while the CO_2 conversion was only improved at ratios above 20 vol%, due to the water–gas shift reaction taking place. The peak production rates of CO and H_2 aligned at 40 vol% CH_4 in the presence of a catalyst, producing *ca.* 24.4 mol mol_{Ni}^{-1} min^{-1}. The minimum EC obtained was around 0.24 MJ mol^{-1}, which is by far the lowest reported EC for post-plasma-catalytic DRM in literature. While the presence of a catalyst did not improve the EC when using a set CH_4/CO_2 ratio, the produced syngas ratio (H_2/CO) was increased with catalyst present for 10–30 vol% CH_4 at the inlet. We also performed a long plasma-catalytic run of 6 h at 30 vol% CH_4, exhibiting stable conversion values and syngas ratio, demonstrating the capability of this post-plasma-catalytic DRM on an extended timescale. Overall, our work demonstrates a significant improvement with respect to other post-plasma-catalytic DRM results reported to date, through a combination of the post-plasma catalyst bed design and the structured catalyst design. The successful identification and characterization of a suitable thermal catalyst, which results in a net positive effect in a post-plasma-catalytic bed, reveals the benefits of bridging the gap between these two aligned fields.

Author contributions

Colin O'Modhrain: conceptualization, methodology, validation, formal analysis, investigation, writing – original draft, project administration. Arturo Pajares: conceptualization, methodology, validation, formal analysis, investigation, writing – original draft, writing – review & editing. Eduardo Coutino-Gonzales: methodology, validation, formal analysis, investigation. Yoran de Vos: methodology, validation, formal analysis, investigation. Yury Gorbanev: validation, formal analysis, investigation, writing – review & editing. Pablo Guardia: methodology, validation, resources, writing – review & editing. Bart Michielsen: validation, resources, writing – review & editing, project administration, funding acquisition. Annemie Bogaerts: methodology, validation, formal analysis, investigation, resources, writing – review & editing, project administration, funding acquisition.

Data availability

The data supporting this article have been included as part of the ESI.†

Conflicts of interest

There are no conflicts to declare.

Acknowledgements

The authors gratefully acknowledge the financial support by the VLAIO-Catalisti ICON project "BluePlasma" (grant ID HBC.2022.0445) and the European Research Council (ERC) under the European Union's Horizon 2020 research and innovation programme (grant agreement No 810182 – SCOPE ERC Synergy project). P.G acknowledge the financial support from MCIN/AEI/10.13039/501100011033 and from FSE+ within the Ramón y Cajal (RYC2022-035588-I and RYC2019-028414) programs.

Notes and references

1 K. Wittich, M. Krämer, N. Bottke and S. A. Schunk, *ChemCatChem*, 2020, **12**, 2130–2147.
2 H. Zhu, H. Chen, M. Zhang, C. Liang and L. Duan, *Catal. Sci. Technol.*, 2024, **14**, 1712–1729.
3 R. K. Parsapur, S. Chatterjee and K. W. Huang, *ACS Energy Lett.*, 2020, **5**, 2881–2885.
4 M. Lu, X. Zhang, J. Deng, S. Kuboon, K. Faungnawakij, S. Xiao and D. Zhang, *Catal. Sci. Technol.*, 2020, **10**, 4237–4244.
5 J. M. Ginsburg, J. Piña, T. El Solh and H. I. De Lasa, *Ind. Eng. Chem. Res.*, 2005, **44**, 4846–4854.
6 J. Yu, T. Le, D. Jing, E. Stavitski, N. Hunter, K. Lalit, D. Leshchev, D. E. Resasco, E. H. Sargent, B. Wang and W. Huang, *Nat. Commun.*, 2023, **14**, 1–9.
7 L. Wu, X. Xie, H. Ren and X. Gao, *Mater. Today: Proc.*, 2021, **42**, 153–160.
8 X. Liu, L. Zhang, X. Zheng, Y. Zhang, D. He and Y. Luo, *Int. J. Hydrogen Energy*, 2022, **47**, 30937–30949.
9 M. Trueba and S. P. Trasatti, *Eur. J. Inorg. Chem.*, 2005, 3393–3403.
10 R. Snoeckx and A. Bogaerts, *Chem. Soc. Rev.*, 2017, **46**, 5805–5863.
11 A. Bogaerts and E. C. Neyts, *ACS Energy Lett.*, 2018, **3**, 1013–1027.
12 H. Hosseini, *RSC Adv.*, 2023, **13**, 28211–28223.
13 K. Li, S. Chen, H. Guo, M. Li, L. Zhong, Q. Sun and F. Wang, *IEEE Trans. Plasma Sci.*, 2024, **52**, 2180–2187.
14 Y. Gorbanev, I. Fedirchyk and A. Bogaerts, *Curr. Opin. Green Sustainable Chem.*, 2024, **47**, 100916.
15 R. De Meyer, Y. Gorbanev, R. G. Ciocarlan, P. Cool, S. Bals and A. Bogaerts, *Chem. Eng. J.*, 2024, **488**, 150838.
16 C. Ndayirinde, Y. Gorbanev, R. G. Ciocarlan, R. De Meyer, A. Smets, E. Vlasov, S. Bals, P. Cool and A. Bogaerts, *Catal. Today*, 2023, **419**, 114156.
17 S. W. Brown, S. Tiwari and J. Hu, *Plasma Processes Polym.*, 2024, **21**, e2400050.
18 S. Tiwari, S. A. Ibrahim, B. Robinson, S. Brown, Q. Wang, F. Che and J. Hu, *Catal. Sci. Technol.*, 2023, **13**, 2966–2981.
19 G. Chen, V. Georgieva, T. Godfroid, R. Snyders and M. P. Delplancke-Ogletree, *Appl. Catal., B*, 2016, **190**, 115–124.
20 M. Młotek, J. Sentek, K. Krawczyk and K. Schmidt-Szałowski, *Appl. Catal., A*, 2009, **366**, 232–241.
21 K. Li, J. L. Liu, X. S. Li, X. Zhu and A. M. Zhu, *Chem. Eng. J.*, 2016, **288**, 671–679.
22 Q. F. Lin, Y. M. Jiang, C. Z. Liu, L. W. Chen, W. J. Zhang, J. Ding and J. G. Li, *Energy Rep.*, 2021, **7**, 4064–4070.
23 X. Tao, F. Qi, Y. Yin and X. Dai, *Int. J. Hydrogen Energy*, 2008, **33**, 1262–1265.
24 Y. Xu, Q. Wei, H. Long, X. Zhang, S. Shang, X. Dai and Y. Yin, *Int. J. Hydrogen Energy*, 2013, **38**, 1384–1390.
25 Z. A. Allah and J. C. Whitehead, *Catal. Today*, 2015, **256**, 76–79.
26 F. Zhu, H. Zhang, X. Yan, J. Yan, M. Ni, X. Li and X. Tu, *Fuel*, 2017, **199**, 430–437.
27 J. L. Liu, Z. Li, J. H. Liu, K. Li, H. Y. Lian, X. S. Li, X. Zhu and A. M. Zhu, *Catal. Today*, 2019, **330**, 54–60.
28 J. Martin-Del-Campo, M. Uceda, S. Coulombe and J. Kopyscinski, *J. CO_2 Util.*, 2021, **46**, 101474.
29 W. Xu, L. C. Buelens, V. V. Galvita, A. Bogaerts and V. Meynen, *J. CO_2 Util.*, 2024, **83**, 102820.
30 B. Wanten, Y. Gorbanev and A. Bogaerts, *Fuel*, 2024, **374**, 132355.
31 C. O'Modhrain, Y. Gorbanev and A. Bogaerts, *J. Energy Chem.*, 2025, **104**, 312–323.
32 T. Nunnally, K. Gutsol, A. Rabinovich, A. Fridman, A. Gutsol and A. Kemoun, *J. Phys. D: Appl. Phys.*, 2011, **44**, 274009.
33 E. Cleiren, S. Heijkers, M. Ramakers and A. Bogaerts, *ChemSusChem*, 2017, **10**, 4025–4036.
34 S. A. Wutzke, E. Pfender and E. R. G. Eckert, *AIAA J.*, 1967, **5**, 707–713.
35 I. Tsonev, C. O'Modhrain, A. Bogaerts and Y. Gorbanev, *ACS Sustainable Chem. Eng.*, 2023, **11**, 1888–1897.
36 B. Wanten, R. Vertongen, R. De Meyer and A. Bogaerts, *J. Energy Chem.*, 2023, **86**, 180–196.
37 Y. Kwon, J. E. Eichler and C. B. Mullins, *J. CO2 Util.*, 2022, **63**, 102112.
38 M. A. Goula, N. D. Charisiou, K. N. Papageridis, A. Delimitis, E. Pachatouridou and E. F. Iliopoulou, *Int. J. Hydrogen Energy*, 2015, **40**, 9183–9200.
39 J. Guo, H. Lou, H. Zhao, D. Chai and X. Zheng, *Appl. Catal., A*, 2004, **273**, 75–82.
40 N. F. P. Ribeiro, R. C. R. Neto, S. F. Moya, M. M. V. M. Souza and M. Schmal, *Int. J. Hydrogen Energy*, 2010, **35**, 11725.
41 R. Wang, Y. Li, R. Shi and M. Yang, *J. Mol. Catal. A: Chem.*, 2011, **344**, 122–127.
42 A. M. Venezia, R. Bertoncello and G. Deganello, *Surf. Interface Anal.*, 1995, **23**, 239–247.
43 L. Sandoval-Diaz, D. Cruz, M. Vuijk, G. Ducci, M. Hävecker, W. Jiang, M. Plodinec, A. Hammud, D. Ivanov, T. Götsch, K. Reuter, R. Schlögl, C. Scheurer, A. Knop-Gericke and T. Lunkenbein, *Nat. Catal.*, 2024, **7**, 161–171.
44 M. Hasegawa, K. Sugawara, R. Suto, S. Sambonsuge, Y. Teraoka, A. Yoshigoe, S. Filimonov, H. Fukidome and M. Suemitsu, *Nanoscale Res. Lett.*, 2015, **10**, 1–6.
45 O. Biondo, K. Wang, H. Zhang and A. Bogaerts, *Chem. Eng. J.*, 2025, **507**, 160190.
46 R. Snoeckx, S. Heijkers, K. Van Wesenbeeck, S. Lenaerts and A. Bogaerts, *Energy Environ. Sci.*, 2016, **9**, 999–1011.
47 M. Ramakers, S. Heijkers, T. Tytgat, S. Lenaerts and A. Bogaerts, *J. CO_2 Util.*, 2019, **33**, 121–130.
48 J. Slaets, M. Aghaei, S. Ceulemans, S. Van Alphen and A. Bogaerts, *Green Chem.*, 2020, **22**, 1366–1377.
49 W. Xu, S. Van Alphen, V. V. Galvita, V. Meynen and A. Bogaerts, *ChemSusChem*, 2024, **17**, e202400169.
50 J. Slaets, E. Morais and A. Bogaerts, *RSC Sustainability*, 2025, **3**, 1477–1493.
51 B. Wanten, S. Maerivoet, C. Vantomme, J. Slaets, G. Trenchev and A. Bogaerts, *J. CO2 Util.*, 2022, **56**, 101869.
52 J. Martin-del-Campo, S. Coulombe and J. Kopyscinski, *Plasma Chem. Plasma Process.*, 2020, **40**, 857–881.
53 S. M. Chun, Y. C. Hong and D. H. Choi, *J. CO_2 Util.*, 2017, **19**, 221–229.